Discovery of shocked H₂ around OH 231.8+4.2

K.P. Forde[1]⋆, T.M. Gledhill[1]

[1] *Centre for Astrophysics Research, University of Hertfordshire, College Lane, Hatfield, AL10 9AB, UK*

ABSTRACT

We present K-band integral field observations of the circumstellar envelope of the evolved star OH 231.8+4.2. Spatial and spectral information were simultaneously acquired using the SINFONI integral field unit, with adaptive optics, on the Very Large Telescope. The observations reveal the discovery of H_2 emission (1) around the centre of the nebula and (2) located in clumps along the Western side of the Northern lobe, presumably associated with the strong shocks that stimulate the previously reported $H\alpha$ emission at the same location. An observed H_2 1→0/2→1S(1) line ratio of 8.3±1.9 was calculated for the central field, a value consistent with shock excitation.

Key words: molecular data – circumstellar matter – stars: AGB and post-AGB – stars: individual(OH 231.8+4.2) – shock waves

1 INTRODUCTION

OH 231.8+4.2 (hereafter OH231) is an O-rich late spectral type (M) central star (Mira variable, QX Pup) with bipolar high-velocity dust and gas outflows (Alcolea et al. 2001), filamentary structures observed in scattered and molecular line emission, and large angular size ($10'' \times 60''$). Often labeled as a post-AGB object or pre-planetary nebula, the presence of both a Mira central star and a main-sequence companion of spectral type A (Sánchez Contreras et al. 2004) seems to contradict this classification. OH231 is more likely a D-type bipolar symbiotic system (Frew & Parker 2010). However in some cases, morphological similarities do exist between post-AGB and symbiotic objects, most strikingly the presence of highly collimated bipolar nebulae. It is via fast-collimated outflows that these stars shape their surrounding nebula. Understanding the development and origin of these fast outflows is critical for advancing hydrodynamical models of wind interaction. Recent work by Lee et al. (2009) attempting to reproduce the high velocity molecular emission in AFGL 618 using collimated fast wind models, emphasises the need for further observations and model development in this area.

OH231 has been the subject of many studies spanning multiple wavelength ranges, for example: Cohen et al. (1985) were first to propose the existence of a binary companion; Bujarrabal et al. (2002) imaged the shape of the shocks using $H\alpha$ (reproduced in Fig. 1 [a]) detected with the *Hubble Space Telescope (HST)*; Meakin et al. (2003) report *HST*/NICMOS NIR images of the dust distribution and hence a high resolution map of the extinction through the nebula. Matsuura et al. (2006) using the MIDI and NACO instruments on the Very Large Telescope (VLT) detected a compact circumstellar disc. The envelope of OH231 is also known to be rich in molecular species (e.g. H_2O, OH, and SiO) however previous studies in the NIR have all returned null detections of H_2 (e.g. Weintraub et al. 1998; Matsuura et al. 2006).

In this Letter, we present the results of preliminary observations of OH231 at NIR (K-band) wavelengths showing for the first time the presence of shock-excited H_2. Throughout this work we assume OH231 is a member of the open cluster M46 at a distance of 1.3 kpc (Jura & Morris 1985). The origin of the coordinate system used in Figures 1,3, and 4 is given by the location of the SiO maser emission at RA=$07^h42^m16^s.93$, Dec=$-14°42'50''.2$ (J2000) (Sánchez Contreras et al. 2002), and the inclination angle of the bipolar axis is $36°$ to the plane of the sky (Kastner et al. 1992).

2 OBSERVATIONS AND DATA REDUCTION

The data were taken using the SINFONI (Eisenhauer et al. 2003) instrument located on UT4 at VLT at Paranal, Chile, on the $1^{st}/2^{nd}$ Feb 2010. We use the lowest resolution mode (LRM), corresponding to the widest field-of-view ($8'' \times 8''$) with adaptive optics (AO) and a natural guide star (NGS). A plate scale of 250×125 mas pixel^{-1}, and a spectral and velocity resolution of 4580 and 66 km s^{-1}, respectively, are available at this resolution (for a dispersion of 2.45 Å/pix and line FWHM of 1.96 pixels). All observations utilised the K-band (2.2 μm) filter which covers many ro-vibrational H_2 emission lines. The ambient seeing varied from ∼ $0.6''$

⋆ E-mail: k.p.forde@herts.ac.uk

Table 1. Details of the VLT/SINFONI observations for OH231 and the telluric standard stars taken on 1st/ 2nd February 2010.

	OH231			HD	
	South	Central	North	75004	63487
Tot. Exp. (secs)	600	600 480	800	1	10
K (mag)	–	– –	–	7.268[†]	7.674[†]
Night	1	1 2	1	1	2

[†] 2mass magnitude from: SIMBAD

to $1.1''$ during the observations. The OH231 observations consisted of three fields focused on (1) the edge of the Northern lobe, (2) the central region, and (3) the middle of the Southern lobe (labelled N, C, S in Fig. 1 [b]). No H_2 was detected in the Southern field and will not be discussed further. Table 1 summarises exposures for each of the three fields. Telluric standard stars used for calibration are HD 75004 (G0V), and HD 63487 (G2V) for night one and two, respectively. An average AO-corrected PSF of $\sim$340 mas FWHM is estimated from the standard stars. The data were reduced using the ESO common pipeline library to a wavelength-calibrated datacube and further analysed using both PyRAF[1]. Wavelength calibration errors were corrected by comparison of OH emission lines with a high resolution template. Quoted velocities were adjusted to local standard of rest (LSR) velocities using 22.88 and 23.30 km s^{-1} corrections for night one and night two, respectively. Line maps (Fig. 1 [c,d]) were generated by fitting the H_2 emission lines with a Gaussian profile; initial fit parameters (FWHM$_0$, central wavelength$_0$, etc.) were determined by manually fitting an individual H_2 line, only lines with a FWHM $\approx$ FWHM$_0$ make up the final line maps. Signal-to-Noise (S/N) of the line maps was enhanced by smoothing the data with a 2×2 pixel boxcar filter. Line rest wavelength information is from Black & van Dishoeck (1987).

3 RESULTS

We report the detection of several H_2 emission lines arising from both the centre and Northern lobe of OH231. In Figure 1 (c,d) we present continuum-subtracted line maps of the $1{\to}0S(1)$ transition for both fields, showing clearly H_2 emission arising from the centre of OH231 (Fig. 1 [d]) and from knots of material in the Northern lobe (Fig. 1 [c]). In Fig. 1 (a) the contours of the detected H_2 are shown in relation to $H\alpha$ emission, while Fig. 1 (b) gives the location of the H_2 relative to the strong continuum emission as imaged with a 2.12 μm filter. An integrated spectrum of the Western region of the centrally located H_2 is shown in Figure 2, from which we note, a) several S- and Q-branch ro-vibrational H_2 lines, and b) a CO bandhead absorption feature ($\sim$2.3 μm).

Channel maps, extracted from the SINFONI datacube, are presented in Figures 3 and 4 for the central and Northern regions respectively, showing how the distribution of the H_2 changes across the line profile.

Table 2 presents the flux measurements for the central and Northern fields, for lines with flux errors less than $\sim$50

Table 2. Line fluxes, F, (in units of 10^{-19} W m^{-2}) of the observed H_2 lines for the central and Northern fields. Measured peak line wavelengths (in μm) are given for the central field.

	Central		Northern
Line	λ_{meas}	F	F
$1{\to}0S(3)$	1.9579	67.2 ± 14.2	11.5 ± 1.10
$1{\to}0S(2)$	2.0342	$9.71 \pm 3.36^{\diamond}$	—
$1{\to}0S(1)$	2.1222	91.5 ± 6.16	9.69 ± 0.76
$2{\to}1S(1)$	2.2481	$7.73 \pm 3.38^{\ddagger}$	—
$1{\to}0Q(1)$	2.4071	46.4 ± 14.5	11.9 ± 2.95
$1{\to}0Q(3)$	2.4241	42.2 ± 24.0	13.3 ± 4.42

[‡] Flux measured for Western H_2 region only.
[◇] Measurement confined to elliptical region (Fig. 1 [d]).

per cent. Accurate $2{\to}1S(3)$, $1{\to}0S(0)$, and $1{\to}0Q(2)$ line flux measurements are not possible due to the presence of strong sky subtraction residuals at these wavelengths. We confine the calculation of the $1{\to}0/2{\to}1S(1)$ ratio for the central field to the area marked by the ellipse in Fig. 1 (d), where the $2{\to}1S(1)$ flux error is smallest. In this region we calculate a $1{\to}0/2{\to}1S(1)$ ratio of 8.3 ± 1.9 prior to extinction correction. We do not detect any $2{\to}1S(1)$ flux in the Eastern H_2 region, instead we estimate an upper $2{\to}1S(1)$ limit (3σ) for the flux in this region of 1.3×10^{-19} W m^{-2}, which in turn places a lower limit of $\sim$9.5 on the $1{\to}0/2{\to}1S(1)$ ratio for this region.

4 ANALYSIS AND DISCUSSION

The $1{\to}0/2{\to}1S(1)$ ratio is a useful discriminator of excitation mechanisms. Pure fluorescence will yield a value of ≈ 2 while a value ≈ 10 indicates the excitation of the gas is being driven by shocks. However it is worth noting, these values depend on shock velocity and pre-shock gas density, with shocked H_2 capable of producing values as low as $\approx$4 (Smith 1995), while fluorescence can produce values approaching those of shocks (Hollenbach & Natta 1995). The $1{\to}0/2{\to}1S(1)$ ratio values, given above, suggest that shocks might be the main excitation mechanism, which agrees with the detection of shock-excited HCO$^+$ in the centre of OH231 noted in the position-velocity diagrams of Sánchez Contreras et al. (2000). In order to determine the intrinsic $1{\to}0/2{\to}1S(1)$ ratio, it is necessary to remove the effects of extinction. In the K-band, it is sometimes possible to derive the level of extinction via the comparison of S-/Q-branch H_2 emission lines (see Smith et al. 2003). Unfortunately, due to poor atmospheric transmission above 2.4 μm, it was not possible to derive a sensible estimate for extinction using the $1{\to}0$ S(1) and Q(3) lines.

Extinction values of A_K=3–4 (mag) for the central region are estimated from the $(K - L')$ colour map of OH231 (Kastner et al. 1998). Although, most likely an overestimate, adjusting the Western $1{\to}0/2{\to}1S(1)$ ratio for these levels of extinction yields, for example, a value of 11.7 ± 2.6 (A_K=4). It is clear that any adjustment for extinction will increase the observed $1{\to}0/2{\to}1S(1)$ ratio, pushing it further towards the shock regime.

Using a typical value of 5.3×10^{-22} mag cm^2 for the extinction per unit column density of hydrogen, $A_V/N(H)$, one can estimate the hydrogen column density implied by an A_K=4; yielding a $N(H)$ for the H_2 regions of $\sim$7.2$\times10^{22}$

---

[1] PyRAF is a product of the Space Telescope Science Institute, which is operated by AURA for NASA.
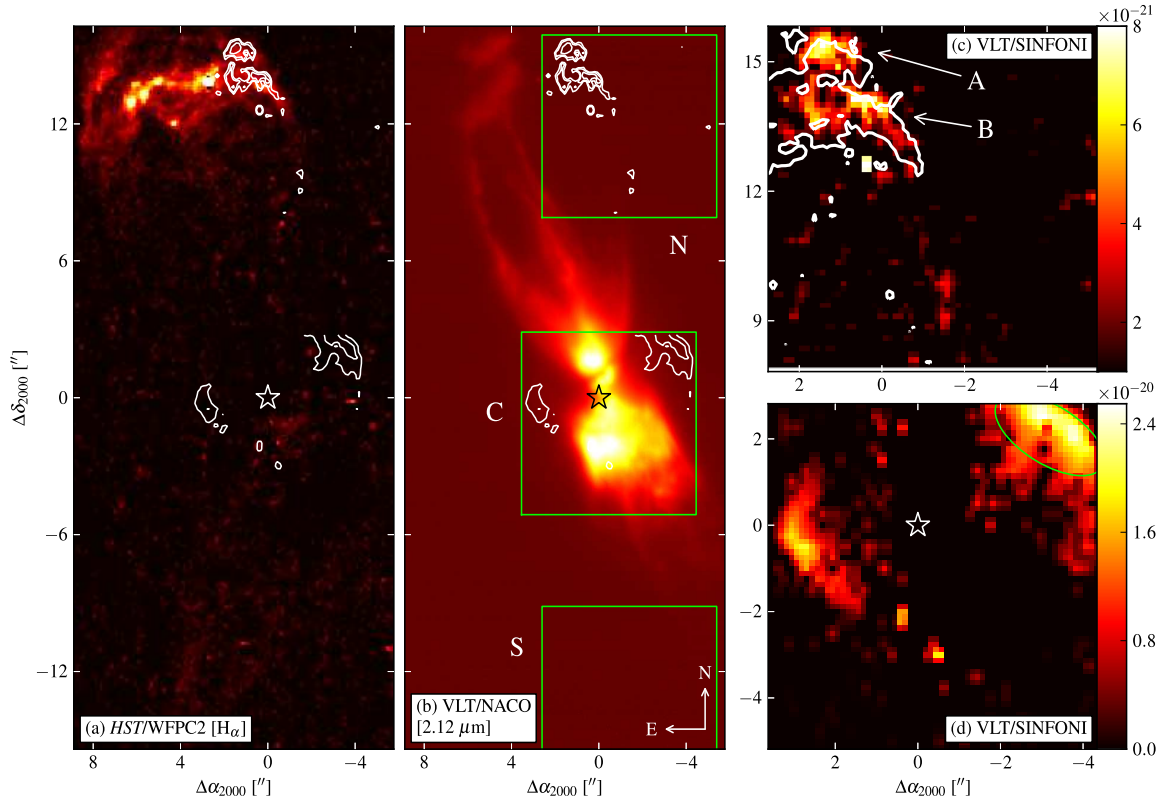
Figure 1. Narrow-band images and line maps for OH231; a star symbol indicates the SiO maser position (see text), inset labels display the telescope/instrument information. (*a*) Continuum-subtracted Hα image with the 1→0S(1) H$_2$ contours overlaid in white, (*b*) 2.12 μm image, showing mainly scattered light, with H$_2$ contours overlaid, SINFONI North, Central, and South (labeled N, C, S) fields are marked by green squares, inset compass shows orientation, (*c*) 1→0S(1) H$_2$ line map showing the extent of the emission located along the edge of the Northern lobe, two knots (A, B) of H$_2$ emission are indicated by arrows; superposed contours indicate the location of the Hα emission, (*d*) 1→0S(1) H$_2$ line map for the central region showing the position/extent of the region used for 1→0/2→1S(1) calculation (ellipse). Colour bar units are in W m^{-2} px^{-1}. The Hα data, from the Hubble Legacy Archive (see Acknowledgments), has been continuum-subtracted using the procedure outlined in Bujarrabal et al. (2002). The 2.12 μm data was first published in Matsuura et al. (2006) and has been reprocessed using the ESO pipeline.

cm^{-2}. Using a typical column length of the H$_2$ emitting regions of $1''(\approx 2.0 \times 10^{16}$ cm), as used in Bujarrabal et al. (2002), we estimate an average density for the H$_2$ regions of 3.5×10^6 cm^{-3}. This value is in good agreement with Alcolea et al. (2001) who estimate an average central density of $\sim 3.0 \times 10^6$ cm^{-3}. The H$_2$ emission is most likely originating in the dense equatorial regions surrounding the central star.

4.1 Equatorial Region

The 1→0S(1) H$_2$ line map (see Fig. 1 [d]) shows two regions of H$_2$ oriented at a position angle (PA) of 113°, from brightest to faintest peak. If we assume that the distribution of the H$_2$ around the central region of OH231 is in a disc configuration then by measuring the major and minor axis we can estimate the inclination angle of the equatorial disc with respect to the plane of the sky from the H$_2$ data. Measurements for R_{max}/R_{min} are determined by superposing a full ellipse onto the H$_2$ line map. We find R_{max}= 4.06″ and R_{min}= 2.76″ from the centre of the ellipse, and using the relation $i = \sin^{-1}(R_{min}/R_{max})$, we find i =43°±8. This result is in good agreement with previously published values.

The location and orientation of this H$_2$ adds to the already complex picture of the equatorial region of OH231. Some previously reported structures, from smallest to largest, include:

- an equatorial torus of SiO maser emission ($\sim$2R$_\star$) that might lie on the innermost edge of an expanding SO disc (Sánchez Contreras et al. 2000, 2002);
- a centrally located compact disc of circumstellar material with inner R=0.03–0.04″/40–50 AU (Matsuura et al. 2006);
- an opaque flared disc with outer R=0.25″/330 AU revealed in mid-IR images (Jura et al. 2002);
- a slowly expanding disc with characteristic R=0.9″/1160 AU, detected via the SO ($J=2_2{\rightarrow}1_1$) transition (Sánchez Contreras et al. 2000);
- a torus of OH maser emission with outer R=2.5″/3250 AU (Zijlstra et al. 2001);
- an expanding hollow cylinder of HCO$^+$ with a characteristic radius equal to the OH torus radius (Sánchez Contreras et al. 2000).
- a halo of scattered light at R$\sim$4″/5200 AU (Meakin et al. 2003);

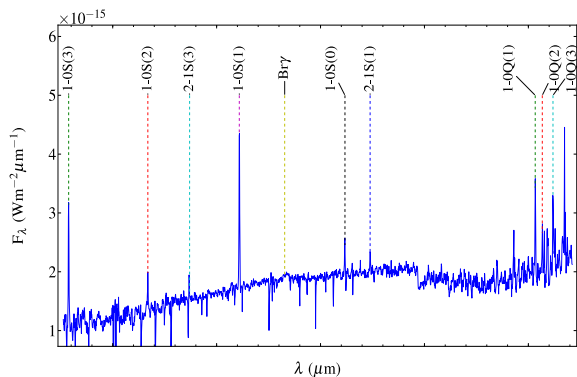From our observations the geometry of the H$_2$ region is un-

Figure 2. An integrated spectrum of the Western side of the central H_2 showing the detected lines, the position of the Brγ recombination line is shown for reference. Extracted spectra location marked in Fig. 1 (d).

clear, however we offer two possibilities: (1) A disc of H_2: Figure 1 (d) shows what might be interpreted as an incomplete disc of H_2, which fits with the series of concentric disc/tori structures listed above. To understand why we observe only emission from the edges and not the front of the disc, a comparison of the noise in the continuum at the front of the putative disc, to the amplitude of the $1\rightarrow0S(1)$ line peak shows both to be of the same order. We might then attribute the 'missing' H_2 in this region to variations in the continuum. We would not expect to observe the back of the disc due to the high level of extinction through the nebula. (2) A shell of H_2: if the H_2 is situated in an axisymmetric shell surrounding the central star, we might explain the geometry of the H_2 regions by assuming a density contrast between the poles and equator. This, combined with an increased column depth at the edge of the shell would manifest itself as two arcs of H_2 emission situated equatorially (as noted by Lowe & Gledhill 2005, for IRAS 19306+1407). This is supported by the detection of a shell of higher density gas and dust at the same location as the H_2 (Meakin et al. 2003). Both scenarios offer plausible explanations for the geometry of the H_2 emitting region, however further observations are needed in order to favour one.

We fit the $1\rightarrow0S(1)$ line profile yielding a $V_{LSR}=36\pm17$ km s^{-1} and FWHM=100 km s^{-1} for both Eastern and Western regions of H_2 emission, a value consistent with the systemic velocity. Channel maps of the $1\rightarrow0S(1)$ line (Fig. 3) show no significant change in the distribution of the H_2.

In an attempt to explain the lack of reported H_2 in this object, we note two previous studies: (1) Weintraub et al. (1998) give a 3σ upper limit of 10^{-5} ergs cm^{-2} s^{-1} ster^{-1} (1σ limit $=6.6\times10^{-18}$ W m^{-2}) for the surface brightness of the $1\rightarrow0S(1)$ line towards OH231. This places their measurement limit close to the $1\rightarrow0S(1)$ line strength given in Table 2, implying that the $1\rightarrow0S(1)$ line in their observations would be difficult to distingush from noise, or possibly that their slit position, aligned East-West across inferred central star position, did not include the H_2 sites; (2) Matsuura et al. (2006), using the ISAAC instrument on VLT, do not report any detection of H_2. However, this can be explained due to the orientation of the slit, aligned from South-
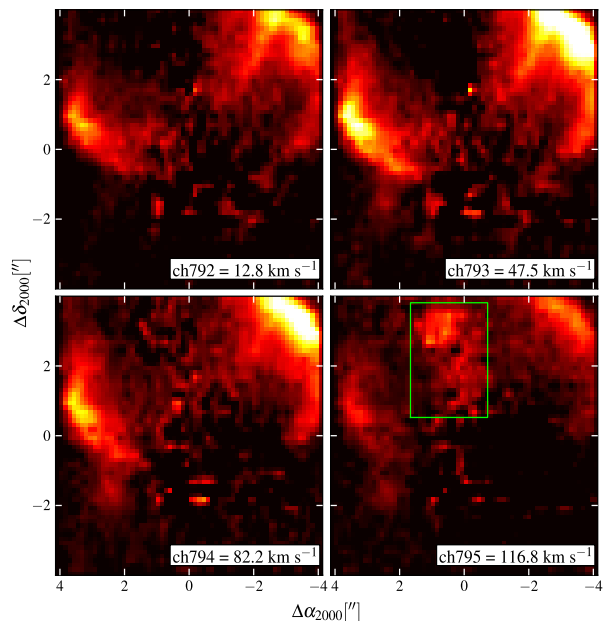

Figure 3. 'Channel maps' of the four central channels of the $1\rightarrow0S(1)$ line from the central region of OH231. Inset labels show datacube channel and corresponding V_{LSR} velocity. Note: in ch794, the central region (marked by a green box) is residual from the continuum subtraction and not true H_2 emission.

West to North-East along the major axis (private comm.), with a slit-width of 0.8″, i.e., the central H_2 emission site was not covered.

4.2 Northern Region

Figure 1 (c) shows the line map for the $1\rightarrow0S(1)$ transition in the Northern region. Most notable are the two knots of H_2, labeled A and B for the top and bottom knot, respectively. The Hα emission contours are superposed on the H_2 line map. The peak intensity of the H_2 emission knots are slightly offset from the two Hα emission knots (Fig. 1 [c]), however this small offset can be accounted for by the motion of the outflow (e.g.$V\sim150$ km s^{-1}, from Bujarrabal et al. 2002) during the 10 years between both sets of observations. It is most likely that the optical and NIR line emission arise from the same shock event. Weaker $1\rightarrow0S(1)$ emission is noted tracing the Hα edge of the bipolar outflow in the lower portion of the $1\rightarrow0S(1)$ line map. The NACO 2.12 μm image does not show any trace of H_2 emission in this region (see contours in Fig. 1 [b]).

The $1\rightarrow0S(1)$ line is spread over $\sim$six spectral pixels, the four central channels are presented in Fig. 4. Examination of the line profile and channel maps allows us to probe the kinematics of the H_2 in this region, revealing two main features: 1) knot B which is persistent in all channel maps 2) the reduction of peak H_2 intensity in knot A at velocities $\leqslant$ -56 km s^{-1}. Both of these H_2 structures lie in the diffuse extended region (labeled B_1 in Fig. 4 of Bujarrabal et al. 2002) perpendicular to the axial flow, with a quoted Hα velocity of 150 km s^{-1} which is in good agreement with not only our deprojected H_2 velocities ($V_{H_2}\sim110$ km s^{-1}) but also with HCO$^+$ velocities (Sánchez Contreras et al. 2000).
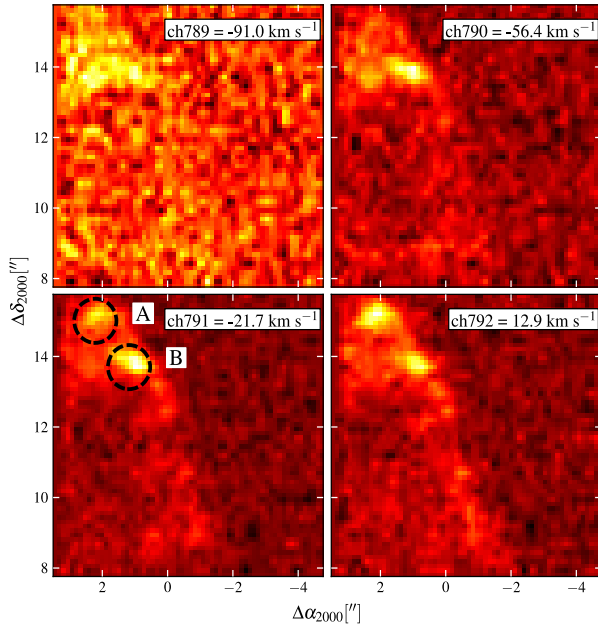
Figure 4. 1→0S(1) line 'channel maps' of the four central channels extracted from the Northern region of OH231. Knot A and B are regions of most intense H$_2$ emission. Labels as in Fig.3.

In the case of knot A, the spectral line is strongly peaked in a single channel, while in knot B the spectral line peak is spread over two channels. Fitting the line profiles of knots A and B, yields LSR velocities of V_{LSR}=-8 km s^{-1}, and -30 km s^{-1}, with deprojected velocities of -75 km s^{-1}and -110 km s^{-1}, respectively. This might indicate that further from the Hα bow apex (Fig. 1 [a]), we are starting to see emission originating from the front and back of knot B, while knot A displays a narrower range of velocities, i.e., a single peak in its spectral profile. It is worth noting that due to the slit-length of ISAAC (120″) coupled with the null H$_2$ detection discussed in §4.1, the H$_2$ in the Northern region might be confined to the wings of the bow shock.

The existence of fast moving shocked H$_2$ has previously been noted in other objects, for example, Cox et al. (2003) detect high velocity H$_2$ ∼220–340 km s^{-1} (dependent on adopted inclination angle) in the outflows of AFGL 618. It is currently unknown exactly how shocked H$_2$ can be travelling at this speed without complete dissociation. Further high resolution mapping of the H$_2$ is necessary in order to resolve the shock surfaces, more accurately measure the H$_2$ kinematics, and apply shock models to this region.

5   CONCLUSIONS

We have presented VLT/SINFONI integral field observations of OH231, revealing the presence of several ro-vibrational H$_2$ lines. The main conclusions are:

- The discovery of H$_2$ emission near the centre of OH231, possibly located at the edge of an axisymmetric shell or an incomplete disc.
- A 1→0/2→1S(1) value of 8.3±1.9 is found for the equatorial H$_2$, suggesting a collisional excitation mechanism.

- Our observations of the central shell/disc of H$_2$ show no velocity structure. However, higher S/N and/or velocity resolution data are needed to accurately probe the kinematics in this region.
- We detect fast-moving H$_2$ (∼110 km s^{-1}, along the bipolar axis) via the 1→0S(1) transition along the North-Western tip of the nebula, a region where a strong Hα bow shock exists. Due to the small FOV of our observations, the full extent of this H$_2$ is unknown.

6   ACKNOWLEDGMENTS

REFERENCES

Alcolea J., Bujarrabal V., Sánchez Contreras C., Neri R., Zweigle J., 2001, A&A, 373, 932
Black J. H., van Dishoeck E. F., 1987, ApJ, 322, 412
Bujarrabal V., Alcolea J., Sánchez Contreras C., Sahai R., 2002, A&A, 389, 271
Cohen M., Dopita M. A., Schwartz R. D., Tielens A. G. G. M., 1985, ApJ, 297, 702
Cox P., Huggins P. J., Maillard J.-P., Muthu C., Bachiller R., Forveille T., 2003, ApJ, 586, L87
Eisenhauer, F. et al., 2003, Proc. SPIE, 4841, 1548
Frew D. J., Parker Q. A., 2010, PASA, 27, 129
Hollenbach D., Natta A., 1995, ApJ, 455, 133
Jura M., Chen C., Plavchan P., 2002, ApJ, 574, 963
Jura M., Morris M., 1985, ApJ, 292, 487
Kastner J. H., Weintraub D. A., Merrill K. M., Gatley I., 1998, AJ, 116, 1412
Kastner J. H., Weintraub D. A., Zuckerman B., Becklin E. E., McLean I., Gatley I., 1992, ApJ, 398, 552
Lee C.-F., Hsu M.-C., Sahai R., 2009, ApJ, 696, 1630
Lowe K. T. E., Gledhill T. M., 2005, ASPC, 343, 282
Matsuura M. et al., 2006, ApJ, 646, L123
Meakin C. A., Bieging J. H., Latter W. B., Hora J. L., Tielens A. G. G. M., 2003, ApJ, 585, 482
Sánchez Contreras C., Bujarrabal V., Neri R., Alcolea J., 2000, A&A, 357, 651
Sánchez Contreras C., Desmurs J. F., Bujarrabal V., Alcolea J., Colomer F., 2002, A&A, 385, L1
Sánchez Contreras C., Gil de Paz A., Sahai R., 2004, ApJ, 616, 519
Smith M. D., 1995, A&A, 296, 789
Smith M. D., Froebrich D., Eislöffel J., 2003, ApJ, 592, 245
Weintraub D. A., Huard T., Kastner J. H., Gatley I., 1998, ApJ, 509, 728
Zijlstra A. A., Chapman J. M., te Lintel Hekkert P., Likkel L., Comeron F., Norris R. P., Molster F. J., Cohen R. J., 2001, MNRAS, 322, 280